Available online at www.sciencedirect.com
ScienceDirect

Comput. Methods Appl. Mech. Engrg. 364 (2020) 112955

Computer methods in applied mechanics and engineering

www.elsevier.com/locate/cma

MAP123-EP: A mechanistic-based data-driven approach for numerical elastoplastic analysis

Shan Tang[a,b,1], Ying Li[c,1], Hai Qiu[a,b], Hang Yang[a,b], Sourav Saha[d], Satyajit Mojumder[d], Wing Kam Liu[e,*], Xu Guo[a,b,**]

[a] State Key Laboratory of Structural Analysis for Industrial Equipment, Department of Engineering Mechanics, Dalian University of Technology, Dalian, 116023, PR China
[b] International Research Center for Computational Mechanics, Dalian University of Technology, 116023, PR China
[c] Department of Mechanical Engineering and Institute of Materials Science, University of Connecticut, Storrs, CT 06269, USA
[d] Theoretical and Applied Mechanics Program, Northwestern University, 60208, USA
[e] Department of Mechanical Engineering, Northwestern University, 60208, USA

Received 18 August 2019; received in revised form 18 February 2020; accepted 19 February 2020
Available online 14 March 2020

Abstract

In this paper, a mechanistic-based data-driven approach, MAP123-EP, is proposed for numerical analysis of elastoplastic materials. In this method, stress-update is driven by a set of one-dimensional stress–strain data generated by numerical or physical experiments under uniaxial loading. Numerical results indicate that combined with the classical strain-driven scheme, the proposed method can predict the mechanical response of isotropic elastoplastic materials (characterized by J2 plasticity model with isotropic/kinematic hardening and associated Drucker–Prager model) accurately without resorting to the typical ingredients of classical model-based plasticity, such as decomposing the total strain into elastic and plastic parts, as well as identifying explicit functional expressions of yielding surface and hardening curve. This mechanistic-based data-driven approach has the potential of opening up a new avenue for numerical analysis of problems where complex material behaviors cannot be described in explicit function/functional forms. The applicability and limitation of the proposed approach are also discussed.

Keywords: Data-driven; Elastoplastic material; Constitutive law; Finite element analysis; Strain-driven

1. Introduction

Most engineering materials, from metal alloys to rocks, are often modeled as elastoplastic material and may experience plastic deformation if the magnitude of the external load they sustain exceeds some critical values. For solving boundary-value problems with elastoplastic materials under conventional paradigm, explicit elastoplastic constitutive laws must be provided to close the problem formulation. Since 1950s, many prominent mechanicians

---

[*] Corresponding author.

[**] Corresponding author at: State Key Laboratory of Structural Analysis for Industrial Equipment, Department of Engineering Mechanics, Dalian University of Technology, Dalian, 116023, PR China.

E-mail addresses: w-liu@northwestern.edu (W.K. Liu), guoxu@dlut.edu.cn (X. Guo).

[1] Equal contribution.

https://doi.org/10.1016/j.cma.2020.112955

such as Hill, Drucker and Prager, developed numerous brilliant plasticity theories [1–4], which help make great successes in understanding the elastoplastic behavior of various types of materials.

With the development of plasticity theory, systematic computational algorithms are proposed to solve the boundary value problem involving elastoplastic materials. Successful implementations of the computational plasticity algorithms are summarized in [5,6], and the references cited therein. These numerical analysis methods are computationally efficient and have been implemented into many commercial softwares. However, conventional numerical analysis on elastoplastic materials is carried out in a model-based paradigm. That is, phenomenological constitutive relationships described in explicit function/functional forms must be employed to describe the physical mechanisms involved in the theory of plasticity, such as yielding function, flow rules, loading/unloading and consistency conditions. This treatment, however, often accompanies the some extent of empiricism and arbitrariness as pointed out in [7].

Apart from conventional model-based approach for computational plasticity, recent years witnessed an increasing attention on developing the data-driven approach for numerical elastoplastic analysis. That is, experimentally/numerically available data is used to solve the corresponding boundary-value problems directly. Liu et al. [8–11] proposed a self-consistent clustering analysis (SCA) method which can be used for modeling of elastoplastic materials. This is a reduced order method capable of decreasing the computational cost significantly through a clustering technique in offline database of elastic response of the materials. Inspired by their works, a FEM-cluster based analysis method (FCA) is also developed in which the cluster-interaction tensors are constructed through finite element analysis avoiding the use of Green's function, further improving the efficiency [12,13]. Recently, Wang et al. [14] proposed a multi-agent meta-modeling approach to generate data, knowledge, and models to make predictions on constitutive responses of elastoplastic materials. In particular, Ortiz and his co-workers proposed a pure model-free data-driven approach in order to bypass the explicit constructions of the constitutive laws from experimental data. It has been demonstrated that this model-free approach is both computationally convenient and numerically robust for nonlinear elastic analysis at small deformation regime [7,15–17]. Also, this model-free approach has also been extended for elastoplastic analysis recently [18]. However, the pure model-free approach may increase the computational cost especially for three-dimensional problems, and is also not compatible with the current strain-driven finite element solver.

Based on the above discussions, it seems natural to develop a data-driven approach, which can fully exploit the deep physical insights obtained from well established plasticity theory and experimental evidence (i.e., mechanistic-based), while at the same time, circumvent the subtle issues of establishing explicit function/functional expressions characterizing material behaviors necessary in classical plasticity theory. If this is the case, one can take both advantages from model-based paradigm and data-driven tools simultaneously. Another issue deserves to be pointed out is that it is usually not an easy task to obtain enough experiment data to characterize constitutive relationships. Even when they are available, many of them are obtained from one dimensional (1D) test. However, in order to solve a 3D problem, we need to construct data sets characterizing the 3D stress/strain state from the available 1D data. To this end, a data-driven approach, coined as MAP123, was proposed for constructing 3D data from 1D data directly for numerical analysis of isotropic nonlinear elastic materials [19,20]. This data-driven technique assumes the coaxial relationship of deviatoric stress and strain, and is capable of describing the nonlinear elastic behavior of materials reasonably well. However, this MAP123 data-driven approach is only applicable for nonlinear elastic analysis and cannot be used to predict elastoplastic responses.

Based on the above consideration, a so-called MAP123-EP approach is proposed to solve boundary-value problems involving isotropic elastoplastic materials. The unique feature of this approach is that although the essential concepts in classical plasticity theory such as material yielding and hardening are preserved, the decomposition of the total strain into elastic and plastic parts, the construction of explicit yielding surface and hardening functions, which are indispensable subtle issues in conventional elastoplastic theories, are totally circumvented. This is achieved by searching two sets of 1D data sets characterizing effective/mean stress–strain relations, which can be generated through either physical or numerical experiments (implemented using the classical strain-driven numerical solution scheme). In this sense, the proposed MAP123-EP can be classified as a type of mechanistic-based data-driven approach, which can not only exploit the deep physical insights inherited from model-based plasticity theory, but also take the advantages provided by data-driven modeling techniques.

The rest of the paper is organized as follows. In Section 2, the framework of the proposed mechanistic-based data-driven computational plasticity approach is established. The data generation procedure is described and the

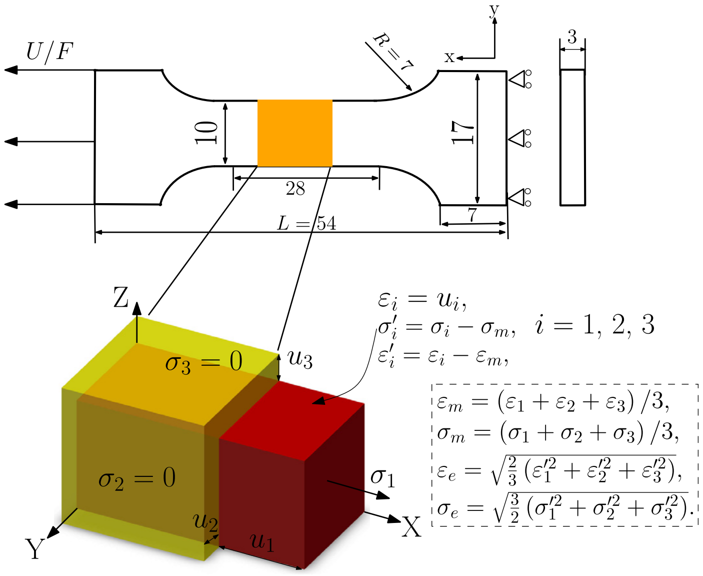

Fig. 1. The specimen used to generate the 1D experiment data under uniaxial tensile loading. The undeformed and deformed configurations of the specimen are plotted in yellow and red colors, respectively. All values of ε_e, σ_e, ε_m, and ε_m can be measured through the designed experiment. (For interpretation of the references to color in this figure legend, the reader is referred to the web version of this article.)

theoretical aspects of the approach are also discussed. The numerical implementation details are then presented in Section 3. Section 4 shows the results of several problems solved using the proposed approach and discusses its accuracy. Concluding remarks are presented in Section 5, where the pros and cons of the proposed MAP123-EP approach are also discussed.

2. The framework of the MAP123-EP approach

This section is centered around a discussion on the fundamental aspects of the MAP123-EP approach. Actually, obtaining 1D data is the basis of MAP123-EP. This 1D data can be generated either by physical experiment or numerical simulation using model-based plasticity theory. The key ingredient of the proposed MAP123-EP approach is to employ this 1D data for numerical elastoplastic analysis. Hence, the generation of appropriate data is of cardinal importance for the successful application of the MAP123-EP approach. In the following, we shall discuss how to generate required data for data-driven numerical analysis.

2.1. Data generation and preprocessing

To demonstrate the capability of the proposed MAP123-EP approach, an Al–Cu alloy is employed to generate the 1D data experimentally. We refer the readers to Gao et al. [21,22,23] for details on the fabrication process of this alloy. The standard dog-bone specimen for tensile experiments is fabricated as shownin Fig. 1a. Digital Image Correlation (DIC) facility is employed to record the displacement of the specimen during the tensile experiments.

The 1D data sets of equivalent strain vs. equivalent stress (ε_e, σ_e) and mean strain vs. mean stress (ε_m, σ_m) can be generated in the following manner within small deformation regime. During the experiments, the strain is recorded as the total strain since it is not necessary to distinguish its elastic and plastic parts in the proposed approach. For the specimen under uniaxial tension, only the region at its center is taken out for analysis, as shown in Fig. 1. The region can be assumed as a 1 × 1 × 1 cube without loosing generality. Under uniaxial tension, the strains can be computed from the measured displacements as $\varepsilon_1 = u_1$, $\varepsilon_2 = u_2$, and $\varepsilon_3 = u_3$. Because of the symmetry, the computed strains in y and z directions are equal ($\varepsilon_2 = \varepsilon_3$). During the tensile experiment, the reaction force F can also be recorded by the testing machine. With the known cross sectional area A of the specimen, the Cauchy stress can be computed as $\sigma_1 = F/A$, $\sigma_2 = \sigma_3 = 0$. Therefore, the mean stress is $\sigma_m = \sigma_1/3$. The value of σ_1 at evenly

Table 1
Parameters chosen for the generation of 1D numerical uniaxial tension/compression non-dimensional data set using J2 plasticity model with isotropic hardening.

Parameter (non-dimensional)	Data set M_A (inclusions)	Data set M_B (matrix)
Elastic modulus, E	5000	1000
Poisson's ratio, ν	0.3	0.3
Yield stress, σ_Y	2	1
Hardening coefficients, K^p	10	3

loading step can be stored in a one-dimensional array: σ_1^n, $n = 1, \ldots, N_s$, where N_s denotes the total number of loading steps. Similarly, the strain components ε_1, ε_2, and ε_3 can be stored as ε_1^n, ε_2^n, and ε_3^n, $n = 1, \ldots, N_s$. From these values, the equivalent strain and stress can be computed and stored as ε_e^n and σ_e^n, $n = 1, \ldots, N_s$, respectively. Likewise, ε_m and σ_m can be computed and stored as ε_m^n and σ_m^n, $n = 1, \ldots, N_s$, respectively. With the procedure described above, two sets of data shown in Fig. 2a are generated. These two sets of data will be used to carry out data-driven simulations on a voided specimen made from the aforementioned alloy. The details of the simulations will be reported in Section 4.

The Young's modulus and Poisson's ratio of the alloy can be obtained through the fitting of the experimental data at initial deformation regime by assuming isotropic elasticity. For the Al–Cu alloy considered in this work, the Young's modulus and Poisson's ratio are calculated to be 63061 MPa and 0.32, respectively.

The data generation process can also be performed through numerical simulations. A material model is required to characterize the material behavior where constitutive relationships are described by explicit functions. In this work, J2 plasticity model is employed as a demonstration. The details of the numerical implementation of J2 plasticity model are given in Appendix B. Besides J2 plasticity model, other plasticity models such as Drucker–Prager model can also be used. Two sets of data $(\varepsilon_e, \sigma_e)$ (called M_A) and $(\varepsilon_m, \sigma_m)$ (called M_B) are generated from numerical simulations, as shown in Fig. 3a and b, respectively, from uniaxial experiments. The parameters chosen for the generation of data sets M_A and M_B using J2 plasticity model are given in Table 1. The exact definitions of these parameters are mentioned in Appendix B.

2.2. *Theoretical aspects*

This section provides a succinct description of the theoretical aspects of the proposed MAP123-EP approach. For detailed derivations, the readers are referred to Appendix A. The proposed MAP123-EP approach uses measured or computed 1D data to update the stress for each incremental step.

The proposed MAP123-EP approach is illustrated as follows. It is assumed that $\boldsymbol{\sigma}^n$ and strains $\boldsymbol{\varepsilon}^n$ at the incremental step n are known. This implies that ε_e^n, ε_m^n and σ_e^n, σ_m^n are also known before the next stress update at step $n+1$ (see, Fig. 2).

Under the displacement-driven framework, the strain increments $\Delta\boldsymbol{\varepsilon}$ are given by the gradient over the increment of displacements $\Delta\mathbf{u}$ from step n to $n+1$:

$$\Delta\boldsymbol{\varepsilon} = \mathrm{sym}(\nabla(\Delta\mathbf{u})). \tag{1}$$

The strain $\boldsymbol{\varepsilon}$ at step $n+1$ is given by

$$\boldsymbol{\varepsilon}^{n+1} = \boldsymbol{\varepsilon}^n + \Delta\boldsymbol{\varepsilon}. \tag{2}$$

The superscript $n+1$ of $\boldsymbol{\varepsilon}^{n+1}$ is dropped for simplification from now on. The equivalent strain and the mean strain are defined as

$$\varepsilon_e = \sqrt{\frac{2}{3}\boldsymbol{\varepsilon}' : \boldsymbol{\varepsilon}'}, \tag{3}$$

and

$$\varepsilon_m = \frac{1}{3}\mathrm{trace}(\boldsymbol{\varepsilon}), \tag{4}$$

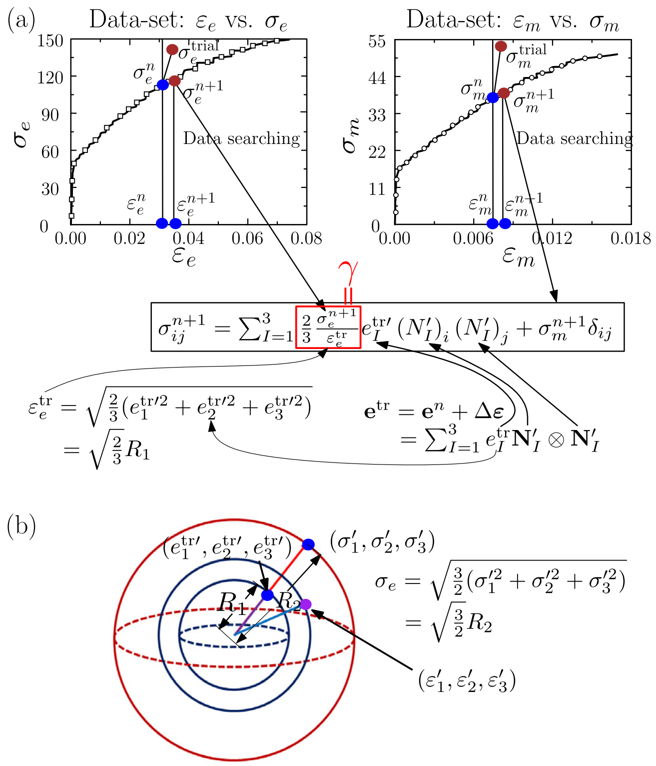

Coaxial relationship of elastic trial strain and stress in principal space

Fig. 2. (a) Two 1D data sets (ε_e, σ_e) and (ε_m, σ_m) generated by physical experiments of uniaxial tension, which are employed to solve boundary-value problems *without any assumed elastoplastic material laws in prior* for the problem shown in Fig. 4. (b) The coaxial relationship between the elastic trial stress and strain are shown in principal stress/strain space. This figure also illustrates how to perform stress-update with the use of the generated data in finite element analysis.

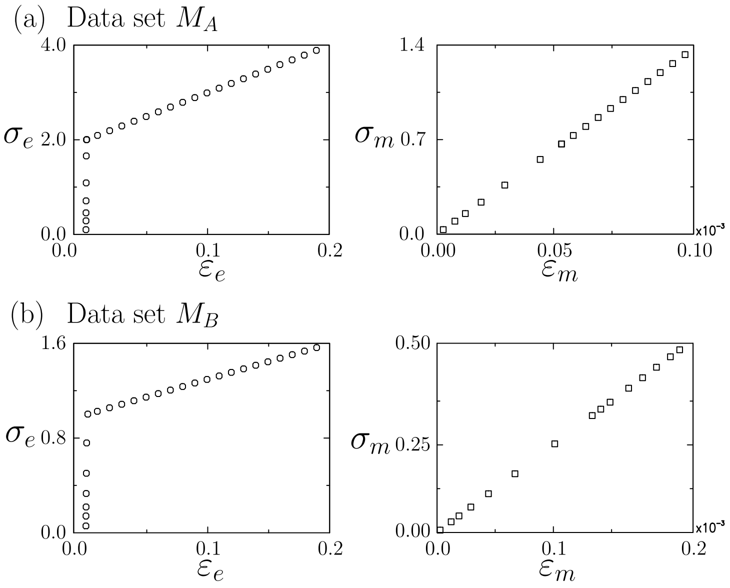

Fig. 3. Two sets of 1D data (ε_e, σ_e) and (ε_m, σ_m) generated by numerical experiments of uniaxial tension with J2 plasticity model, called M_A and M_B. These data sets are employed to solve boundary-value problems *without any assumed explicit elastoplastic material laws in prior*.

where $\boldsymbol{\varepsilon}'$ is the deviatoric part of $\boldsymbol{\varepsilon}$. The elastic trial strain is introduced as

$$\mathbf{e}^{\mathrm{tr}} = \mathbf{e}^{n} + \Delta\boldsymbol{\varepsilon}, \tag{5}$$

where $\mathbf{e}^{n}$ is the elastic strain at the incremental step n, which can be computed from $\boldsymbol{\sigma}^{n}$ as

$$\mathbf{e}^{n} = \left(\mathbf{C}^{e}\right)^{-1} : \boldsymbol{\sigma}^{n}, \tag{6}$$

where $\mathbf{C}^{e}$ is the fourth order elasticity tensor of isotropic material.

The spectral decomposition of the elastic trial strain is given by

$$\mathbf{e}^{\mathrm{tr}} = \sum_{I=1}^{3} e_{I}^{\mathrm{tr}} \mathbf{N}'_{I} \otimes \mathbf{N}'_{I}, \tag{7}$$

where e_{I}^{tr} and $\mathbf{N}'_{I}$, $I = 1, 2, 3$, are the eigenvalues and the corresponding eigenvectors of $\mathbf{e}^{\mathrm{tr}}$, respectively. Mapping the data from 1D to 3D harnesses the coaxial relationship between the deviatoric elastic trial strain and deviatoric Cauchy stress (see Appendix C for a proof). A visualization of this relationship is provided in Fig. 2b. In addition, σ_{e} can be found (marked as σ_{e}^{n+1} in Fig. 2) by searching the experimental data set $(\varepsilon_{e}^{l},\ \sigma_{e}^{l})$, $l = 1,\ \ldots,\ N_{s}$. Then, the parameter γ is obtained as

$$\gamma = \frac{2}{3} \frac{\sigma_{e}}{\varepsilon_{e}^{\mathrm{tr}}}, \tag{8}$$

where $\varepsilon_{e}^{\mathrm{tr}}$ is the effective elastic trial strain. The physical meaning of γ can be seen in Fig. 2b. Similarly, the mean stress σ_{m} at each Gauss point can be found from σ_{m}^{l}, $l = 1,\ \ldots,\ N_{s}$, by matching the computed ε_{m} in the data of ε_{m}^{l}, $l = 1,\ \ldots,\ N_{s}$, marked on the right part of Fig. 2a. Finally, due to the coaxial relationship between the Cauchy stress and elastic trial strain, the Cauchy stress on the loading path can be computed as:

$$\sigma_{ij} = \sum_{I=1}^{3} \gamma e_{I}^{\mathrm{tr}\prime} \left(N'_{I}\right)_{i} \left(N'_{I}\right)_{j} + \sigma_{m}\delta_{ij}, \tag{9}$$

where $e_{I}^{\mathrm{tr}\prime}$, $I = 1, 2, 3$, are the eigenvalues of deviatoric part of $\mathbf{e}^{\mathrm{tr}}$, and the symbol $\left(N'_{I}\right)_{i}$ represents the ith component of $\mathbf{N}'_{I}$.

In the present work, two independent conditions on equivalent and mean stresses, respectively, are used to identify the loading/unloading state. In fact, these two conditions should be correlated. However, taking them as independent ones is a practical way to achieve data-driven simulations using 1D experimental data efficiently. Numerical results shown in Section 4 indicate that this treatment can reproduce experimental results within a reasonable accuracy.

The plastic softening can also be considered in the proposed framework if the one-dimensional data can characterize the corresponding deformations. Under this circumstance, new experimental techniques should be developed for data generation. Further works are needed along this direction.

Remarks. I. The stress update in MAP123-EP is different from that in classical computational plasticity. There is no explicit decomposition of the total strain into its elastic and plastic parts in the present data-driven approach. Furthermore, the flow rule, hardening law, and the yielding surface with explicit mathematical forms are totally avoided.

II. This section only sheds some light on how to update stress under the elastic or plastic loading cases. The unloading cases will be discussed in detail in the subsequent numerical implementation section.

III. Under uniaxial tension or compression along the x direction, it is evident that $\sigma_{11} \neq 0$ and $\sigma_{22} = \sigma_{33} = 0$. Therefore, $\sigma_{m} = \sigma_{11}/3$. However, it also holds that $\varepsilon_{11} \neq \varepsilon_{22}$, $\varepsilon_{11} \neq \varepsilon_{33}$ and $\varepsilon_{22} = \varepsilon_{33} \neq 0$. Hence, the experiments should also measure the strains in the y and z directions too. Only measuring ε_{11} is not enough to compute the effective and the mean strains.

IV. It should be noted that the proposed approach cannot be applied to anisotropic elastoplastic materials, as proved in Appendix C. More efforts are needed to deal with anisotropic elastoplastic materials through the data-driven approach.

V. The proposed MAP123-EP tries not to be a totally model-free approach. It still uses the insights from the model-based plasticity theory. Firstly, since plastic deformation is history and loading-path dependent, MAP123-EP

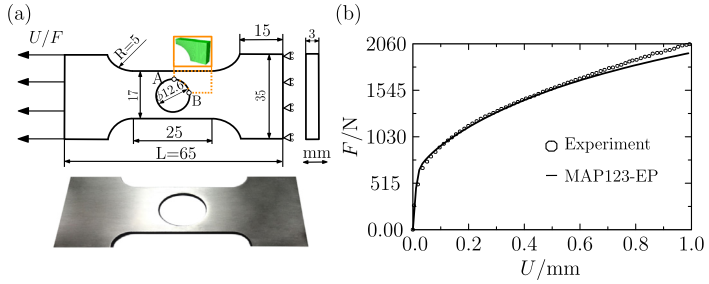

Fig. 4. (a) A specimen with a single hole at its center under tensile loading. The dimension of the specimen is described in Fig. 4a. A prescribe displacement U is imposed on its left side and the reaction force F on its right side is calculated. This problem is solved by the data-set generated by the uniaxial tension experiment of a standard homogeneous Aluminum alloy specimen, shown in Fig. 2. (b) The reaction force vs. the imposed displacement obtained by the proposed MAP123-EP method and physical experiments, respectively.

updates stress in a step-wise fashion. Secondly, although the yielding function is not involved in the MAP123-EP, it is implicitly assumed that the yield function depends on the mean as well as equivalent stresses, and the plastic flow is (yielding surface) associated. Thirdly, the judgment on the loading/unloading paths also resorts to trial stress concept in classical computational plasticity. In this sense, the proposed data-driven approach is coined as “mechanistic-based”.

3. Numerical implementation

The numerical implementation of MAP123-EP is carried out within the displacement-driven finite element framework. At the outset, in order to perform stress-update and compute the internal force vector, a C^0 displacement interpolation is adopted. The interpolation is constructed based on the displacement $\mathbf{u}^A$ at node through the shape function $\bar{N}^A$. With the available information from step n, the stress-update algorithm is described in Box 1. Unless otherwise stated, the superscript $n+1$ is dropped for the quantity at the step $n+1$. From the description of the algorithm, one can see that unlike in classical computational plasticity implementation, the MAP123-EP approach does not use the return-mapping algorithm for stress update. The stress at step $n+1$ is obtained by searching the data set directly (see Fig. 2). A trial stress is introduced to identify whether the material point is in loading or unloading condition by comparing the value of σ_e^{n+1} (σ_e^{tr}) and σ_m^{n+1} (σ_m^{tr}). This is necessary since MAP123-EP does not use an analytical expression of yield surface. After stress update, the residual force vector and the tangent stiffness matrix can be calculated accordingly [6]. Note that the 1D stress–strain data is generated in a discrete form. This makes it difficult to obtain the analytical derivatives necessary for the construction of tangent stiffness matrix. However, the tangent stiffness matrix can be computed numerically. Actually, after the stress is updated, the corresponding stiffness matrix can be constructed by taking the numerical derivatives of the stress with respect to strain approximately with the use of finite difference operations.

4. Numerical results and discussion

In this section, we will demonstrate the effectiveness of the proposed MAP123-EP approach by solving several problems involving elastoplastic behaviors. Experimentally generated 1D uniaxial tensile data is used in the first problem, while numerically generated 1D data are used for the solution of the remaining three problems.

4.1. Results obtained using the experimentally generated data

In order to verify the efficacy of the MAP123-EP approach, we have performed physical experiments and numerical simulations using MAP123-EP, respectively, on a voided Aluminum alloy specimen shown in Fig. 4a. To apply MAP123-EP, the data shown in Fig. 2a generated by the uniaxial tension test is used as the source 1D data. Dimensional details of the voided specimen (made of the same type of Aluminum alloy) are also described in Fig. 4a. The uniaxial tensile experiment is carried out by a universal testing machine and a DIC testing facility

1. **Data collection:** $\{\boldsymbol{\sigma}^n, \boldsymbol{\varepsilon}^n\}$ and two one-dimensional data sets $([\varepsilon_e], [\sigma_e])$ and $([\varepsilon_m], [\sigma_m])$.
2. **Compute the total strain $\boldsymbol{\varepsilon}$ and strain increment $\Delta\boldsymbol{\varepsilon}$ at every Gauss point X_g:**

   $$\varepsilon_{ij}\big|_{X_g} = \left.\frac{\partial \bar{N}^A}{\partial x_j}\right|_{X_g} u_i^A,$$

   $$\Delta\varepsilon_{ij}\big|_{X_g} = \left.\frac{\partial \bar{N}^A}{\partial x_j}\right|_{X_g} \Delta u_i^A.$$

3. **Compute the elastic strain $\mathbf{e}^n$ at step n:**

   $$e_{ij}^n\big|_{X_g} = \left(C^e\right)^{-1}_{ijkl}\,\sigma^n_{kl}\big|_{X_g}.$$

4. **Compute the elastic trial strain $\mathbf{e}^{\mathrm{tr}}$:**

   $$e_{ij}^{\mathrm{tr}}\big|_{X_g} = e^n_{ij}\big|_{X_g} + \Delta\varepsilon_{ij}\big|_{X_g}.$$

5. **Compute the eigenvalues and eigenvectors of $\mathbf{e}^{\mathrm{tr}}|_{X_g}$**

   $$\mathbf{e}^{\mathrm{tr}}\big|_{X_g} \Rightarrow \begin{cases} e_I^{\mathrm{tr}}, I = 1, 2, 3, \\ \mathbf{N}_I, I = 1, 2, 3, \end{cases}$$

   where e_I^{tr} and $\mathbf{N}_I$, $I = 1, 2, 3$, are the eigenvalues and eigenvectors of $\mathbf{e}^{\mathrm{tr}}$, respectively.
6. **Compute the effective trial strain $\varepsilon_e^{\mathrm{tr}}$:**

   $$e_m^{\mathrm{tr}} = \frac{1}{3}\left(e_1^{\mathrm{tr}} + e_2^{\mathrm{tr}} + e_3^{\mathrm{tr}}\right),$$

   $$e_I^{\mathrm{tr}\prime} = e_I^{\mathrm{tr}} - e_m^{\mathrm{tr}} \text{ and } \varepsilon_e^{\mathrm{tr}} = \sqrt{\frac{2}{3} e_I^{\mathrm{tr}\prime} e_I^{\mathrm{tr}\prime}}.$$

7. **Compute the effective total strain ε_e and the mean strain ε_m:**

   $$\varepsilon_m = \frac{1}{3}\left(\varepsilon_{11} + \varepsilon_{22} + \varepsilon_{33}\right),$$

   $$\varepsilon'_{ij} = \varepsilon_{ij} - \varepsilon_m \text{ and } \varepsilon_e = \sqrt{\frac{2}{3}\varepsilon'_{ij}\varepsilon'_{ij}}.$$

8. **Search one-dimensional data $(\varepsilon_e, \sigma_e)$ to obtain γ:**

   $$\gamma = \frac{2}{3}\left.\frac{\sigma_e}{\varepsilon_e^{\mathrm{tr}}}\right|_{X_g}.$$

9. **Search one-dimensional data $(\varepsilon_m, \sigma_m)$ to obtain σ_m.**
10. **Compute the deviatoric and hydrostatic parts of stress $\boldsymbol{\sigma}^L$ on the plastic loading path:**

    $$\left(\sigma_{ij}^L\right)^{\mathrm{dev}}\Big|_{X_g} = \sum_{I=1}^{3} \gamma \varepsilon_I^{\mathrm{tr}\prime} \left(N_I\right)_i \left(N_I\right)_j,$$

    $$\sigma_m^L\big|_{X_g} = \sigma_m.$$

    where $\left(\sigma_{ij}^L\right)^{\mathrm{dev}}$ and σ_m^L represent the deviatoric and hydrostatic parts of the stress on the elastic/plastic loading path, respectively.

Box 1. Algorithm for stress update in MAP123-EP.

11. **Compute the trial stress:**

$$\sigma_{ij}^{\mathrm{tr}} = \sigma_{ij}^{n}\big|_{X_g} + C_{ijkl}^{e}\ \Delta\varepsilon_{kl}\big|_{X_g}\ .$$

12. **Compute the effective and hydrostatic trial stress:**

$$\sigma_m^{\mathrm{tr}} = \frac{1}{3}\left(\sigma_{11}^{\mathrm{tr}} + \sigma_{22}^{\mathrm{tr}} + \sigma_{33}^{\mathrm{tr}}\right),$$

$$\left(\sigma_{ij}^{\mathrm{tr}}\right)^{\mathrm{dev}} = \sigma_{ij}{}^{\mathrm{tr}} - \sigma_m^{\mathrm{tr}},$$

$$\sigma_e^{\mathrm{tr}} = \sqrt{\frac{3}{2}\left(\sigma_{ij}^{\mathrm{tr}}\right)^{\mathrm{dev}}\left(\sigma_{ij}^{\mathrm{tr}}\right)^{\mathrm{dev}}}.$$

13. **Loading–unloading condition:**

```
IF  $\sigma_e^{\mathrm{tr}} \geq \sigma_e^L$   THEN
        $\sigma_{ij}^{\mathrm{dev}} = \left(\sigma_{ij}^L\right)^{\mathrm{dev}}$        (Loading)
ELSE
        $\sigma_{ij}^{\mathrm{dev}} = \left(\sigma_{ij}^{\mathrm{tr}}\right)^{\mathrm{dev}}$   (Unloading)
END IF
IF  $\mathrm{abs}\left((\sigma_m)^{\mathrm{tr}}\right) \geq \mathrm{abs}\left(\sigma_m^L\right)$   THEN
        $\sigma_m = \sigma_m^L$              (Loading)
ELSE
        $\sigma_m = \sigma_m^{\mathrm{tr}}$            (Unloading)
END IF
```

$$\sigma_e^L = \sqrt{\frac{3}{2}\left(\sigma_{ij}^L\right)^{\mathrm{dev}}\left(\sigma_{ij}^L\right)^{\mathrm{dev}}}.$$

14. **Update stress according to the loading–unloading condition:**

$$\sigma_{ij} = \sigma_{ij}^{\mathrm{dev}} + \sigma_m\delta_{ij}.$$

Box 1. (*continued*).

is used to record the deformation of the specimen at each loading step around the void area. The displacement and the corresponding reaction force are plotted in Fig. 4b.

Numerical simulations of the same problem are then performed by the proposed MAP123-EP approach. Considering the symmetry, only one-eighth of the specimen is used to build FE model and three dimension eight-node elements are employed for finite element analysis. Fig. 4b plots the reaction force vs. displacement relation obtained from the data-driven simulation and experiment, respectively. It indicates that the results obtained by MAP123-EP agree well with the experimental results at small deformation regime. However, under large deformation, the prediction by MAP123-EP deviates from the experimental evidence. This result is expected because the proposed MAP123-EP approach is actually developed under the assumption of small deformation.

To further verify the performance of MAP123-EP, the deformed configuration of the specimen predicted by MAP123-EP is also compared with the experimental evidence at several values of imposed displacement (see Fig. 5a). The shapes of the void predicted by the MAP123-EP match well with the experiment evidences. Furthermore, the results provided in Fig. 5b also indicate that the predicted values of u_A^y and u_B^x also agree well with the experiment results. These results confirm the effectiveness and accuracy of the proposed MAP123-EP approach at small deformation regime.

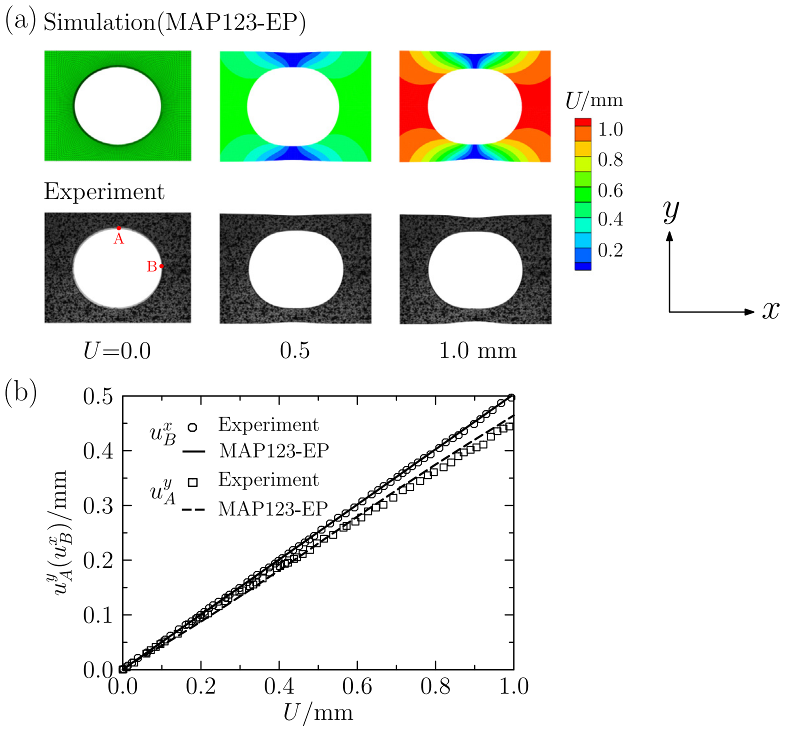

Fig. 5. (a) Deformed configurations of the specimen at different levels of imposed displacement (i.e., $U = 0$, 0.5, and 1.0 mm respectively), obtained by the proposed MAP123-EP approach and experiments, respectively. (b) A comparison of the values of the displacements at point A (y direction) and point B (x direction) obtained by MAP123-EP and experimental measurement, respectively.

4.2. Results obtained using numerically generated data

To further illustrate the effectiveness of the MAP123-EP approach, numerically generated 1D data are also employed to solve some example problems, and the results are verified by the numerical solutions obtained from the implementation of classical J2 plasticity model. In these examples, the numerically generated uniaxial tensile test data set shown in Fig. 3 is used for the MAP123-EP based simulation. Two problems are solved by MAP123-EP: a square plate with circular inclusions and a square plate with circular holes. For the first problem shown in Fig. 6a, a square plate ($1 \times 1 \times 0.1$) with circular inclusions (radius 0.05) is investigated. The left and bottom surfaces of the plate are fixed and prescribed displacement is applied on its right surface. The imposed displacement increases linearly from 0 to 0.01 and then decreases to zero. The material data associated with the matrix and inclusion materials are represented by the data sets M_A and M_B, respectively. We also solved the same problem using the classical return mapping algorithm with both the matrix and the inclusion materials are described by J2 plasticity model. The parameters of the J2 plasticity models are taken from the data sets M_A and M_B, respectively. The values of these parameters are summarized in Table 1.

Fig. 6b plots the average stress vs. the average strain for the considered problem obtained by both MAP123-EP and J2 plasticity model based numerical simulations. The average stress (F_R/A) is defined as the reaction force over the cross sectional area of right surface where the prescribed displacement is applied. The average strain is defined as the displacement over the original length of the square plate (U/L). It can be seen clearly that the average stress–strain response predicted by MAP123-EP is almost the same as that predicted using the classical J2 plasticity model.

Fig. 7 plots the contours of the effective stress σ_e under three levels of strain $U/L = 7.8 \times 10^{-4}$, 1×10^{-2} and 9×10^{-3}, corresponding to points I and II and III on the stress–strain curves shown in Fig. 6b for both models. At states I, II, and III, the structure is under elastic loading, plastic loading and elastic unloading, respectively, in terms of conventional plasticity theory. It can be observed from Fig. 7 that the stress distributions are almost the same between MAP123-EP and the classical J2 model.

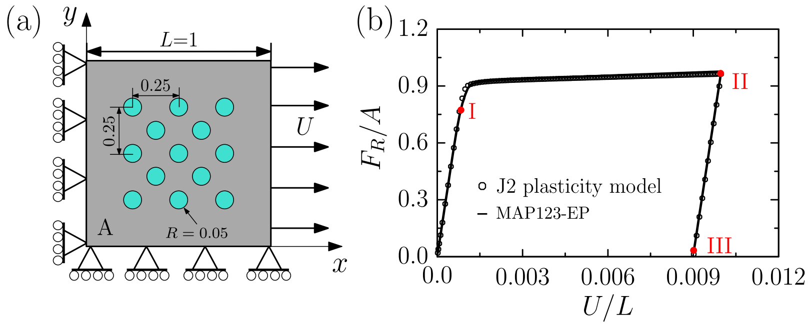

Fig. 6. A square plate with distributed circular inclusions. (a) A schematic illustration of the considered problem. (b) The average stress–strain curves predicted by the reference J2 plasticity model and the proposed MAP123-EP approach, respectively.

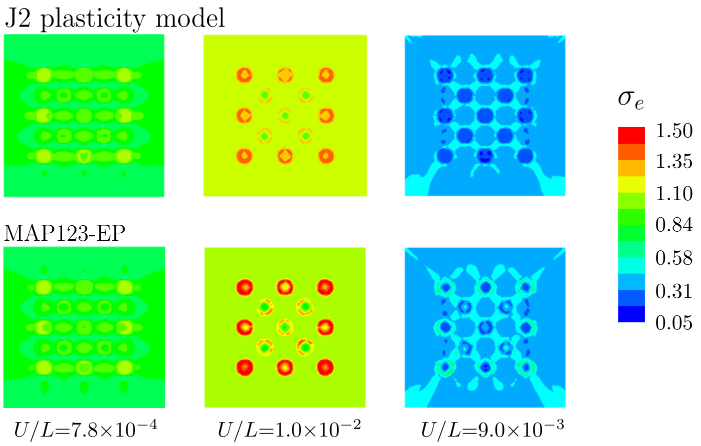

Fig. 7. Contour plots of the effective Cauchy stress predicted by MAP123-EP and the reference J2 plasticity model at three levels of imposed strain $U/L = 7.8 \times 10^{-4}$, 1×10^{-2}, and 9×10^{-3}, respectively. The corresponding strain–stress states are also marked as I, II, III, respectively, in Fig. 6a.

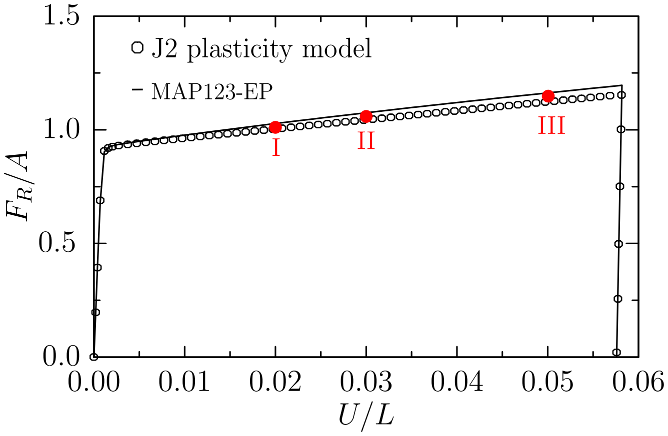

Fig. 8. Average stress–strain curves obtained by the reference J2 plasticity model and the proposed MAP123-EP considering large strain for the problem shown in Fig. 6a.

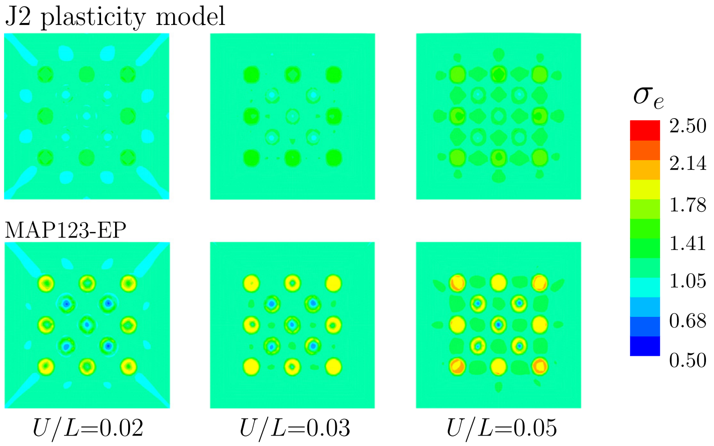

Fig. 9. Contour plots of the effective stress field predicted by MAP123-EP and the reference J2 plasticity model at three levels of imposed strain $U/L = 2 \times 10^{-2}$, 3×10^{-2} and 5×10^{-2}, respectively. The corresponding strain–stress states are also marked as I, II, III, respectively, in Fig. 8.

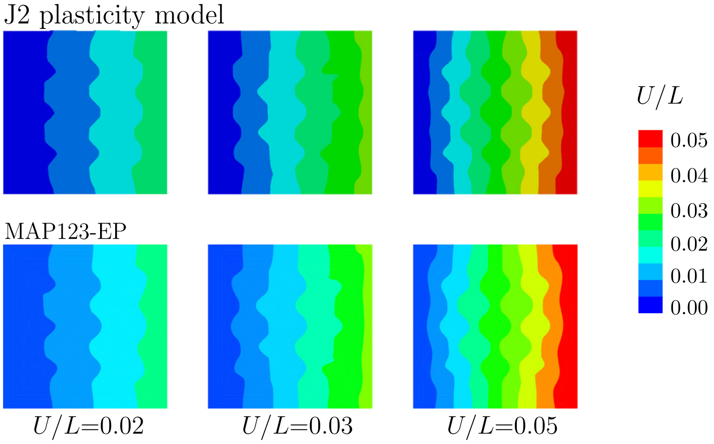

Fig. 10. Contour plots of the displacement fields predicted by MAP123-EP method and the reference J2 plasticity model under three levels of imposed strain $U/L = 1 \times 10^{-2}$, 2×10^{-2} and 5×10^{-2}, respectively. The corresponding strain–stress states are also marked as I, II, III, respectively, in Fig. 8.

Now we investigate the same problem shown in Fig. 6a with a larger magnitude of applied strain (i.e., $\varepsilon = 0.06$). The predicted stress–strain curves are shown in Fig. 8. The differences in the average stress between the results obtained by MAP123-EP and J2 plasticity model are within 5% even at large strain. It should be noted here that the data of the *effective (mean) stress vs. effective (mean) strain* are used to perform the stress update, which is not the same as that in the model-based J2 plasticity model where the explicit relationship between the *flow stress and effective plastic strain* is required. This may cause the difference observed in Fig. 8 at relatively large deformation. Three different strain levels (marked as I, II, and III) are picked from the average stress–strain plot and the corresponding displacement contours are shown for both models in Fig. 10. It can be observed that the displacement contours for both models are quite similar. However, the predicted stress contours at the considered strain levels (i.e., $U/L = 0.02$, 0.03 and 0.05, respectively) show somewhat differences (see Fig. 9). Noted that the present method is developed under the small deformation assumption.

We now consider a square plate ($1 \times 1 \times 0.1$) with circular holes of radius 0.05 to test the performance of MAP123-EP. The geometric setup and boundary conditions are shown in Fig. 11a. The displacement U is applied on the right surface and the maximum displacement is 0.01. After that, the unloading starts and the prescribed displacement decreases to zero gradually. For this problem, the left surface of the square plate is fixed in both x

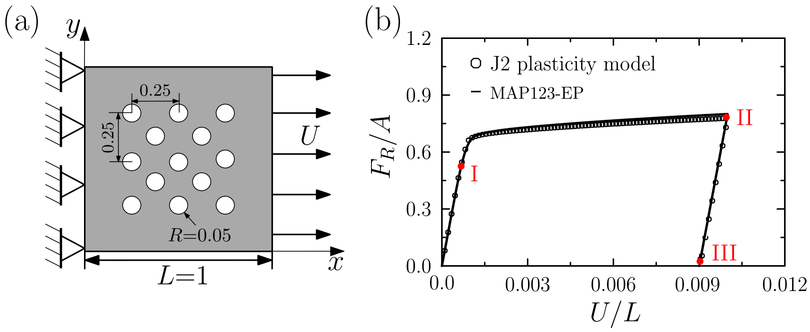

Fig. 11. A square plate with distributed circular holes. (a) A schematic illustration of the considered problem. (b) The average stress–strain curves obtained by the reference J2 plasticity model and the proposed MAP123-EP approach.

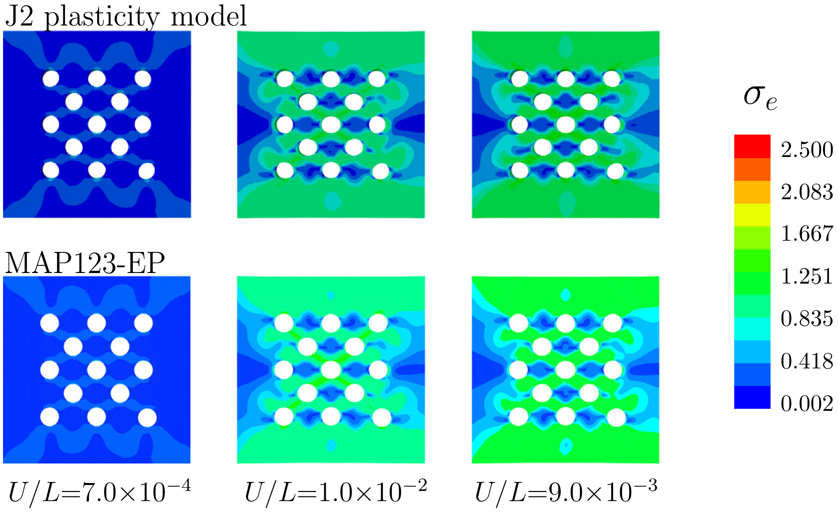

Fig. 12. Contour plots of the effective stress field predicted by MAP123-EP method and the reference J2 plasticity model at three levels of imposed strain $U/L = 7 \times 10^{-4}$, 1×10^{-2} and 9×10^{-3}, respectively. The corresponding strain–stress states are also marked as I, II, III, respectively, in Fig. 11b.

and y directions. The front and back surfaces are fixed in the z direction. For solving this problem, both reference J2 plasticity model and the proposed MAP123-EP approach are used. For the implementation of MAP123-EP, the 1D data set of M_B (see Fig. 3) is used. Fig. 11b shows the average stress vs. strain results predicted by MAP123-EP.

Fig. 12 presents the contour of the effective stress predicted by the reference J2 plasticity model and the proposed MAP123-EP approach under three different strain levels (i.e., $U/L = 7 \times 10^{-4}$, 1×10^{-2}, and 9×10^{-3}, respectively, corresponding to the points I, II, and III on the stress–strain curves shown in Fig. 11b). It can be seen that the stress contours are quite similar predicted by both the reference J2 plasticity model and the proposed MAP123-EP approach.

Previous examples only compare the MAP123-EP approach with the classical J2 plasticity model under two-dimensional conditions. We finally test MAP123-EP with a more complicated 3D problem, where the involved material behavior can be described by the associated Drucker–Prager model. The same way is adopted to generate the stress–strain data as in the previous examples. The values of the parameters for the considered Drucker–Prager material model are given in Table 2. The generated 1D data by numerical simulation is shown in Fig. 13. We then build a FE model for a cubic specimen with a spherical hole (radius 0.05) locating at its center, shown in Fig. 14a. The x, y, z degrees of freedom of the left surfaces are fixed. The displacement U is imposed on the right surface. The remaining surfaces are set to be traction free. Both the reference associated Drucker–Prager model and the proposed MAP123-EP approach are employed for numerical simulations. Fig. 14b shows the stress vs. engineering

Table 2
Parameters chosen for the generation of 1D numerical uniaxial tension/compression non-dimensional data set using the associated Drucker–Prager plasticity model with isotropic hardening.

Parameter (non-dimensional)	Data set (only for matrix material)
Elastic modulus, E	1000
Poisson's ratio, ν	0.3
Yield stress, σ_Y	1
Hardening coefficients, K^p	20
Pressure sensitivity coefficients, β, ψ	0.2

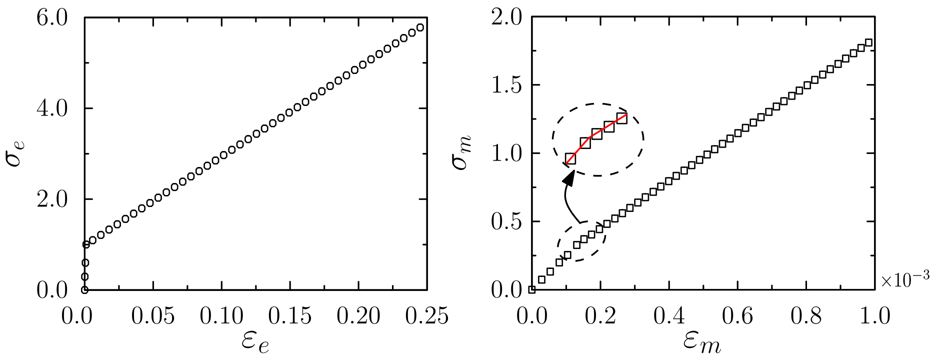

Fig. 13. (a) Generated 1D data sets (ε_e, σ_e) and (ε_m, σ_m) by numerical simulations of uniaxial tension with associated Drucker–Prager model, which are employed to solve the 3D problem shown in Fig. 14.

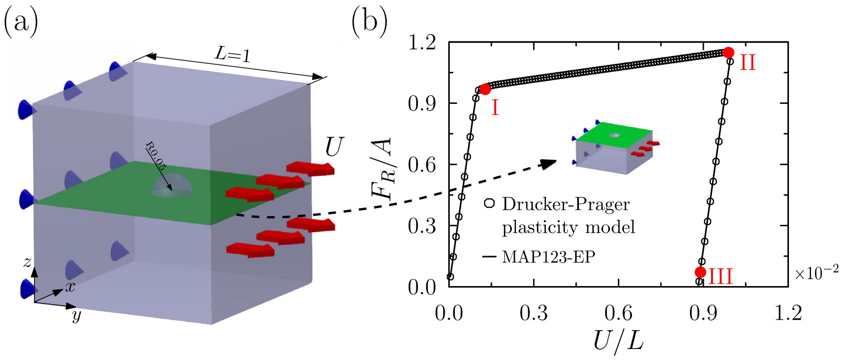

Fig. 14. A cube with a spherical hole. (a) A schematic illustration of the considered problem. (b) The average stress–strain curves obtained by the reference associated Drucker–Prager plasticity model and the proposed MAP123-EP approach. (For interpretation of the references to color in this figure legend, the reader is referred to the web version of this article.)

strain curves for both cases. The average stress is defined as F_R/A, where F_R is the reaction force along x direction on the right surface of the specimen, and A is the cross sectional area of the right surface before deformation. The engineering strain is defined as U/L. An excellent agreement between results obtained by the two approaches is clearly observed at small deformation regime. Fig. 15 plots the effective stress contour on the section of green surface (see Fig. 14) at different strain levels (i.e., 7.0×10^{-4}, 1.0×10^{-2}, 8.9×10^{-3}, respectively, marked as I, II and III in Fig. 14b). It indicates that the stress distribution predicted by MAP123-EP is almost the same as that of the reference Drucker–Prager model.

To examine how the data set can affect the simulation results, we run the simulations with 200, 500 and 1000 data points by the proposed MAP123-EP approach. The same way is used to generate these data as in other examples. The corresponding computational times are 632, 686 and 709 s of wall-clock time, respectively. The simulation based on reference Drucker–Prager model takes 165 s of wall-clock time. The computational time associated with

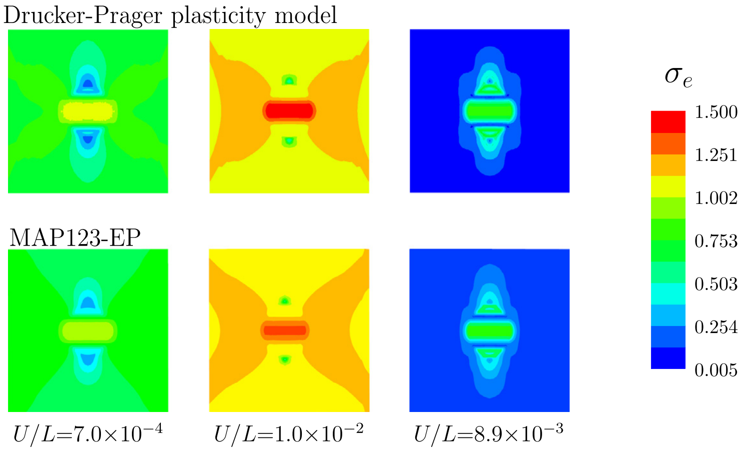

Fig. 15. Contour plots of the effective stress field (section marked by green in Fig. 14) predicted by MAP123-EP and the reference associated Drucker–Prager plasticity model at three levels of imposed strain $U/L = 7 \times 10^{-4}$, 1×10^{-2} and 9×10^{-3}, respectively. The corresponding strain–stress states are also marked as I, II, III, respectively, in Fig. 14.

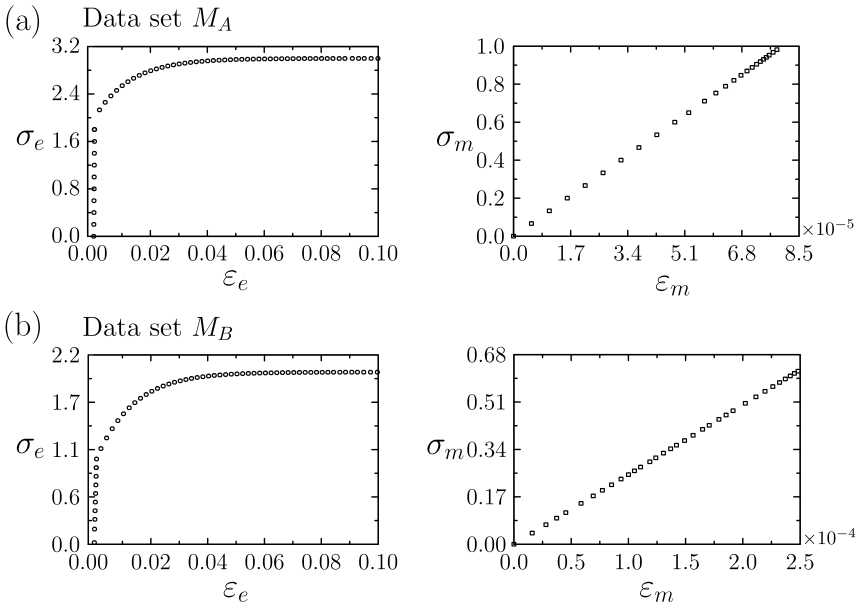

Fig. 16. Two generated sets of 1D data (ε_e, σ_e) (called M_A) and (ε_m, σ_m) (called M_B) by numerical simulations where the J2 plasticity model with nonlinear kinematic hardening is adopted. These two data sets are employed to solve the problems shown in Fig. 6a.

MAP123-EP is longer than that of the reference model because the calculation of the tangent stiffness matrix takes more time if only discrete data points are used for computation. The obtained results with different data points are almost the same, which are not shown here to save space.

Besides isotropic hardening case shown above, we also solve the same problem with nonlinear kinematic hardening. The same way illustrated in Section 2.1 is employed to generate the data sets for inclusion and matrix materials, called M_A and M_B, respectively. The data-sets are shown in Fig. 16. The material parameters used for generating the 1D data sets (M_A, and M_B) corresponding to the kinematic hardening law are given in Table 3. The same problem shown in Fig. 6a is studied with these newly generated data sets. Fig. 17 plots the average stress vs. the average strain for both cases. It can be seen clearly that the stress–strain response predicted by MAP123-EP is almost the same as that predicted by the classical J2 plasticity model with nonlinear kinematic hardening law.

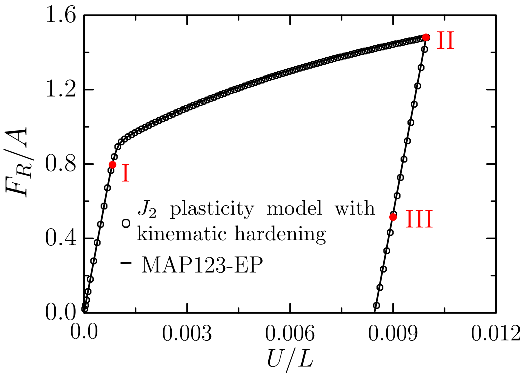

Fig. 17. The average stress–strain curves for the square plate with inclusions predicted by the reference J2 plasticity model with kinematic hardening and the proposed MAP123-EP approach.

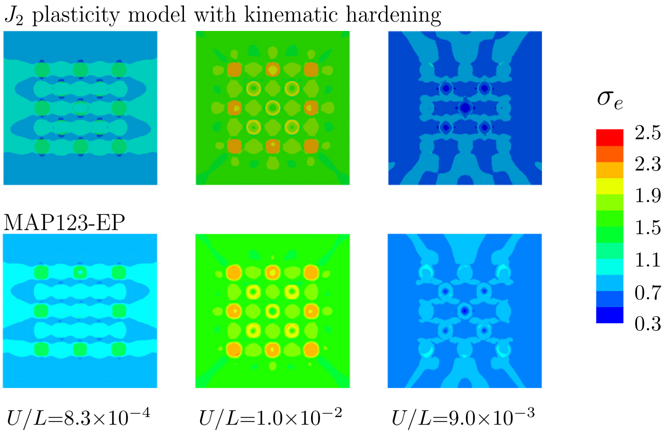

Fig. 18. Contour plots of the effective stress field predicted by MAP123-EP and the reference J2 plasticity model with kinematic hardening at three levels of imposed strain $U/L = 8.3 \times 10^{-4}$, 1×10^{-2} and 9.0×10^{-3}, respectively. The corresponding strain–stress states are also marked as I, II, III, respectively, in Fig. 17.

Table 3

Parameters used for the generation of the 1D numerical data set characterizing J2 plasticity model with kinematic hardening.

Parameter (non-dimensional)	Data set M_A (inclusions)	Data set M_B (matrix)
Elastic modulus, E	5000	1000
Poisson's ratio, ν	0.3	0.3
Yielding stress, σ_Y	2	1
Hardening coefficient, γ_1	80	80
Hardening coefficient, C_1	80	80

Fig. 18 plots the contour of the effective stress σ_e at three levels of strain (i.e., $U/L = 8.3 \times 10^{-4}$, 1×10^{-2} and 9×10^{-3} respectively, corresponding to the points I, II and III on the stress–strain curves shown in Fig. 17). It should be noted here that although the nonlinear kinematic hardening behavior can be captured by MAP123-EP, however, MAP123-EP cannot be used to consider cyclic/reverse loading in its present form.

5. Conclusions

In this paper, a mechanistic-based data-driven MAP123-EP approach is proposed for numerical elastoplastic analysis. Compared with traditional model-based paradigm, the proposed data-driven computational framework offers an opportunity to predict the mechanical responses of isotropic elastoplastic materials without knowing the explicit functional forms of the constitutive descriptions characterizing the material behaviors. Only two sets of data generated (either numerically or experimentally) under uniaxial loading are required for numerical implementation. It is found that this approach predicts the elastoplastic behavior reasonably well when compared with the experimental results and the results obtained through conventional model-based paradigm. Furthermore, the MAP123-EP approach is also consistent with the classical strain-driven approach for computational plasticity. In addition, compared with pure model-free approach, it is easier to be implemented in conventional finite element analysis softwares.

In the present work, the effectiveness of the proposed approach is only validated through numerical experiments. Rigorous analyses on the well-posedness of the corresponding boundary value problem formulation, the stability and convergence properties of the proposed data-driven numerical solution scheme still lacks. The framework and tools developed in [7,15–18] for data-driven based solution of elastic problems may be very helpful for the theoretical analysis of the proposed approach. It is also worth noting that the MAP123-EP approach is not a pure model-free approach since some basic concepts in classical plasticity model established from physical mechanisms/insights are still adopted. How to construct pure model-free paradigms for numerical elastoplastic analysis (we refer the readers to Kirchdoerfer and Ortiz [7] for the first attempt on this aspect) is still a very challenging problem and deserves serious investigations.

It is important to point out that the proposed MAP123-EP approach relies on the assumption that the yield function depends on the mean as well as equivalent stresses, and the plastic deformation obeys the associated flow rule. It also cannot be applied for solving problems under cyclic/reverse loading in its present form. There is no doubt that the current version of the approach is not as universal as the existing model-based approaches for elastoplastic analysis. The main purpose of the present work, however, aims at demonstrating the fact that data-driven paradigm is also applicable for elastoplastic analysis with reasonable accuracy and acceptable efficiency under certain conditions. We hope this work can inspire more attractive ideas and subsequent researches in this area.

Acknowledgment

S.T. appreciates the support from NSF of China (Project No. 11872139). X.G. thanks the support from NSF of China (11732004, 11821202), Program for Changjiang Scholars, and Innovative Research Team in University (PCSIRT). S.S., S.M., W.K.L. acknowledged the support of the United States National Science Foundation (NSF) under Grant No. MOMS/CMMI-1762035.

Appendix A. The detailed derivation of MAP123-EP

The spectral decomposition of the symmetric total strain tensor $\boldsymbol{\varepsilon}$ can be written as

$$\boldsymbol{\varepsilon} = \sum_{I=1}^{3} \varepsilon_I \mathbf{N}_I \otimes \mathbf{N}_I, \tag{A.1}$$

where ε_I, $I = 1, 2, 3$, are the eigenvalues of $\boldsymbol{\varepsilon}$ and $\mathbf{N}_I$, $I = 1, 2, 3$, are the corresponding eigenvectors.

The effective strain at small deformation regime is defined by

$$\varepsilon_e = \sqrt{\frac{2}{3}\left(\varepsilon_1'^2 + \varepsilon_2'^2 + \varepsilon_3'^2\right)}, \tag{A.2}$$

$$\varepsilon_I' = \varepsilon_I - \varepsilon_m, \ I = 1,\ 2,\ 3 \tag{A.3}$$

with $\varepsilon_m = (\varepsilon_1 + \varepsilon_2 + \varepsilon_3)/3$.

The Cauchy stress can be decomposed in its spectral forms

$$\boldsymbol{\sigma} = \sum_{I=1}^{3} \sigma_I \mathbf{N}_I' \otimes \mathbf{N}_I', \tag{A.4}$$

where σ_I and $\mathbf{N}_I'$, $I = 1, 2, 3$, are the corresponding eigenvalues and eigenvectors, respectively. Note that in general, the eigenvectors $\mathbf{N}_I'$ are not the same as those of $\mathbf{N}_I$ due to the possible existence of plastic deformation [19].

The effective stress is defined as

$$\sigma_e = \sqrt{\frac{3}{2}\left(\sigma_1'^2 + \sigma_2'^2 + \sigma_3'^2\right)}, \tag{A.5}$$

where

$$\sigma_I' = \sigma_I - \sigma_m, \;\; I = 1,\ 2,\ 3 \tag{A.6}$$

with $\sigma_m = (\sigma_1 + \sigma_2 + \sigma_3)/3$. Then the stress can be expressed by

$$\sigma_{ij} = \sum_{I=1}^{3} \sigma_I' \left(N_I'\right)_i \left(N_I'\right)_j + \sigma_m \delta_{ij}, \tag{A.7}$$

where δ_{ij}, $i,\ j = 1,\ 2,\ 3$, is the Kronecker delta symbol and $(N_I')_i$ is the ith component of $\mathbf{N}_I'$ under the prescribed Cartesian coordinate system.

Introduction of the elastic trial strain $\mathbf{e}^{\mathrm{tr}}$ is the key for MAP123-EP. Actually, $\mathbf{e}^{\mathrm{tr}}$ is defined as

$$\mathbf{e}^{\mathrm{tr}} = \mathbf{e}^n + \Delta\boldsymbol{\varepsilon}, \tag{A.8}$$

where $\mathbf{e}^n$ is the elastic strain at step n. $\mathbf{e}^n$ can be computed from $\boldsymbol{\sigma}^n$ as

$$\mathbf{e}^n = \left(\mathbf{C}^e\right)^{-1} : \boldsymbol{\sigma}^n. \tag{A.9}$$

Here, $\mathbf{C}^e$ is the fourth-order isotropic elasticity tensor. For isotropic elastoplastic materials, $\mathbf{N}_I'$, the eigenvectors of $\mathbf{e}^{\mathrm{tr}}$, are coaxial with stress $\boldsymbol{\sigma}'$ [5,24], that is,

$$\mathbf{e}^{\mathrm{tr}} = \sum_{I=1}^{3} e_I^{\mathrm{tr}} \mathbf{N}_I' \otimes \mathbf{N}_I', \tag{A.10}$$

where e_I^{tr}, $I = 1, \ldots, 3$, are the eigenvalues of $\mathbf{e}^{\mathrm{tr}}$. As shown in Appendix C, it also holds that

$$\frac{\sigma_1'}{e_1^{\mathrm{tr}\prime}} = \frac{\sigma_2'}{e_2^{\mathrm{tr}\prime}} = \frac{\sigma_3'}{e_3^{\mathrm{tr}\prime}} = \gamma, \tag{A.11}$$

where γ reflects the shear modulus of material in terms of physical meaning. Actually, $\gamma = 2\mu$ at the elastic stage with μ denoting the shear modulus. The effective stress can then be rewritten as

$$\sigma_e = \gamma\sqrt{\frac{3}{2}\left(e_1^{\mathrm{tr}\prime 2} + e_2^{\mathrm{tr}\prime 2} + e_3^{\mathrm{tr}\prime 2}\right)} = \frac{3}{2}\varepsilon_e^{\mathrm{tr}}\gamma, \tag{A.12}$$

which immediately leads to

$$\gamma = \frac{2}{3}\frac{\sigma_e}{\varepsilon_e^{\mathrm{tr}}} \tag{A.13}$$

with

$$\varepsilon_e^{\mathrm{tr}} = \sqrt{\frac{2}{3}\left(e_1^{\mathrm{tr}\prime 2} + e_2^{\mathrm{tr}\prime 2} + e_3^{\mathrm{tr}\prime 2}\right)}. \tag{A.14}$$

Harnessing the mapping between $\varepsilon_e^{\mathrm{tr}}$ and ε_e and searching the available data of effective strain in the array of ε_e^l, $l = 1, \ldots, N_s$, the corresponding effective stress can be found in the array of σ_e^l, $l = 1, \ldots, N_s$. Then the deviatoric stress can be calculated directly with the use of Eqs. (A.11) and (A.13). By searching the available data of mean strain in the array of ε_m^l, $l = 1, \ldots, N_s$, the mean stress can also be found in the array of σ_m^l, $l = 1, \ldots, N_s$. Finally, the components of Cauchy stress tensor can be obtained in the following form

$$\sigma_{ij} = \sum_{I=1}^{3} \gamma e_I^{\mathrm{tr}\prime} \left(N_I'\right)_i \left(N_I'\right)_j + \sigma_m \delta_{ij}, \qquad i,\ j = 1,\ 2,\ 3. \tag{A.15}$$

In this way, the measured one-dimensional experimental data in terms of $(\varepsilon_e, \sigma_e)$ and $(\varepsilon_m, \sigma_m)$ can be used to achieve three dimensional stress update.

Appendix B. Basic ingredients in classical J2 plasticity

The classical rate-independent J2 plasticity model under small deformation, which is used for generating the data sets and validating the effectiveness of the proposed MAP123-EP approach, is recapitulated here.

In the classical J2 plasticity model at small deformation regime, the total strain $\boldsymbol{\varepsilon}$ can be decomposed into an elastic part and a plastic part, that is

$$\boldsymbol{\varepsilon} = \boldsymbol{\varepsilon}^e + \boldsymbol{\varepsilon}^p, \tag{B.1}$$

where the superscripts e and p denote the elastic and plastic part, respectively.

The classical J2 plasticity model actually includes the following five key ingredients:

I. The elastic stress–strain relationship can be expressed as

$$\sigma_{ij} = 2\mu\varepsilon_{ij}^{e\prime} + 3K_m\varepsilon_m^e\delta_{ij}, \qquad i,\ j = 1,\ 2,\ 3. \tag{B.2}$$

where $\varepsilon_{ij}^{e\prime}$ is the deviatoric elastic strain and ε_m^e represents spherical elastic strain. In Eq. (B.2), μ and K_m are shear modulus and bulk modulus which can be related with Young's modulus E and Poisson's ratio ν through: $\mu = E/2(1+\nu)$ and $K_m = E/3(1-2\nu)$, respectively.

II. Yielding condition and hardening law:

$$f(\boldsymbol{\sigma}, \alpha) = \|\boldsymbol{\sigma}\| - \left(\sigma_Y + K^p\alpha\right) \le 0, \tag{B.3}$$

where $f(\boldsymbol{\sigma}, \alpha)$ is the so-called yielding function, σ_Y is the initial yielding stress, K^p is the plastic modulus, and α is an internal hardening variable which is usually represented by the accumulated effective plastic strain.

III. Flow rule:

$$\dot{\boldsymbol{\varepsilon}}^p = \Lambda\frac{\partial f}{\partial \boldsymbol{\sigma}}, \tag{B.4}$$

where $\Lambda \geqslant 0$ is the so-called plastic multiplier.

IV. Kuhn–Tucker complementary conditions:

$$\Lambda \geqslant 0; \qquad f(\boldsymbol{\sigma}, \alpha) \le 0; \qquad \Lambda f(\boldsymbol{\sigma}, \alpha) = 0, \tag{B.5}$$

V. Consistency condition:

$$\Lambda\dot{f}(\boldsymbol{\sigma}, \alpha) = 0. \tag{B.6}$$

In addition to isotropic hardening, the nonlinear kinematic hardening is also considered in the present work. In this case, the yielding condition is described by

$$f(\boldsymbol{\sigma}, \boldsymbol{\beta}) = \|\boldsymbol{\sigma} - \boldsymbol{\beta}\| - \sigma_Y \le 0, \tag{B.7}$$

where $\boldsymbol{\beta}$ is the so-called backstress. The evolution of backstress is governed by

$$\dot{\boldsymbol{\beta}} = C_1\dot{\varepsilon}_e^p\frac{(\boldsymbol{\sigma} - \boldsymbol{\beta})}{\sigma_Y} - \gamma_1\boldsymbol{\beta}\dot{\varepsilon}_e^p + \frac{1}{C_1}\boldsymbol{\beta}\dot{C}_1, \tag{B.8}$$

where $\dot{\varepsilon}_e^p$ is the rate of accumulated effective plastic strain while C_1 and γ_1 are two material parameters. We refer the readers to Simo and Hughes [5] for more details.

Appendix C. Coaxial relationship of deviatoric stress and deviatoric strain under strain-driven solution scheme

In this section, the coaxial relationship of deviatoric stress and deviatoric strain is proved. Actually, in conventional plasticity theory, the yielding surface is often described by a function with the mean stress σ_m and effective stress σ_e as its arguments:

$$\Psi = \Psi(\sigma_m, \sigma_e). \tag{C.1}$$

The definitions of the mean stress and effective stress can be found in Appendix A.

The total incremental strain can be decomposed into an elastic and a plastic part as

$$\Delta\boldsymbol{\varepsilon}^{n+1} = \Delta\left(\boldsymbol{\varepsilon}^e\right)^{n+1} + \Delta\left(\boldsymbol{\varepsilon}^p\right)^{n+1}.$$

If a fully implicit backward Euler scheme is adopted for stress integration, we have

$$\begin{aligned}\Delta\left(\boldsymbol{\varepsilon}^{p}\right)^{n+1} &= \Delta\Lambda\frac{\partial\Psi}{\partial\boldsymbol{\sigma}}\\ &= \Delta\Lambda\frac{\partial\Psi}{\partial\sigma_m}\frac{1}{3}\mathbf{1}+\Delta\Lambda\frac{\partial\Psi}{\partial\sigma_e}\frac{3\boldsymbol{\sigma}'}{2\sigma_e},\end{aligned}\tag{C.2}$$

where $\Delta\Lambda$ is the increment of the plastic multiplier and $\mathbf{1}$ is the second order identity tensor. The values of $\partial\Psi/\sigma_m$ and $\partial\Psi/\partial\sigma_e$ are evaluated at step $n+1$ with $\sigma_m=\sigma_m^{n+1}$ and $\sigma_e=\sigma_e^{n+1}$(this assertion is also assumed in the following derivation). Then the elastic trial strain is given by

$$\begin{aligned}\boldsymbol{\varepsilon}^{\mathrm{tr}} &= (\boldsymbol{\varepsilon}^{e})^{n}+\Delta\boldsymbol{\varepsilon}^{n+1}\\ &= (\boldsymbol{\varepsilon}^{e})^{n}+\Delta(\boldsymbol{\varepsilon}^{e})^{n+1}+\Delta(\boldsymbol{\varepsilon}^{p})^{n+1}\\ &= (\boldsymbol{\varepsilon}^{e})^{n}+\Delta(\boldsymbol{\varepsilon}^{e})^{n+1}+\Delta\Lambda\frac{\partial\Psi}{\partial\sigma_m}\frac{1}{3}\mathbf{1}+\Delta\Lambda\frac{\partial\Psi}{\partial\sigma_e}\frac{3\boldsymbol{\sigma}'}{2\sigma_e}\\ &= (\boldsymbol{\varepsilon}^{e})^{n+1}+\Delta\Lambda\frac{\partial\Psi}{\partial\sigma_m}\frac{1}{3}\mathbf{1}+\Delta\Lambda\frac{\partial\Psi}{\partial\sigma_e}\frac{3\boldsymbol{\sigma}'}{2\sigma_e}.\end{aligned}\tag{C.3}$$

The spherical and deviatoric parts of the elastic trial strain can be obtained as

$$\mathrm{trace}\left(\varepsilon^{\mathrm{tr}}\right)=\mathrm{trace}\left(\left(\boldsymbol{\varepsilon}^{e}\right)^{n+1}\right)+\Delta\Lambda\frac{\partial\Psi}{\partial\sigma_m},\tag{C.4}$$

$$\boldsymbol{\varepsilon}^{\mathrm{tr}\prime}=\left(\frac{1}{2\mu}+\Delta\Lambda\frac{\partial\Psi}{\partial\sigma_e}\frac{3}{2\sigma_e}\right)\boldsymbol{\sigma}',\tag{C.5}$$

which indicates clearly that the deviatoric part of elastic trial strain $\varepsilon^{\mathrm{tr}'}$ is coaxial with the deviatoric stress σ'. It is worth noting that if the yielding surface is also dependent on the third invariant of deviatoric stress, the aforementioned co-axiality property does not exist anymore. Under this circumstance, the proposed approach cannot be applied directly and different schemes should be developed for data-driven stress update.

References

[1] R. Hill, The Mathematical Theory of Plasticity, Oxford University Press, 1998.

[2] R. Hill, J.R. Rice, Constitutive analysis of elastic-plastic crystals at arbitrary strain, J. Mech. Phys. Solids 20 (6) (1972) 401–413.

[3] D.C. Drucker, W. Prager, Soil mechanics and plastic analysis or limit design, Quart. Appl. Math. 10 (2) (1952) 157–165.

[4] Y.C. Fung, D.C. Drucker, Fundation of solid mechanics, Acta Mech. Solida Sin. 33 (1) (1980) 238.

[5] J.C. Simo, T.J. Hughes, Computational Inelasticity, Vol. 7, Springer Science & Business Media, 2006.

[6] T. Belytschko, W.K. Liu, B. Moran, Nonlinear Finite Elements for Continua and Structures, John Wiley and Sons Inc., 2014.

[7] T. Kirchdoerfer, M. Ortiz, Data driven computational mechanics, Comput. Methods Appl. Mech. Engrg. 304 (2016) 81–101.

[8] Z. Liu, J.A. Moore, S.M. Aldousari, H.S. Hedia, S.A. Asiri, W.K. Liu, A statistical descriptor based volume-integral micromechanics model of heterogeneous material with arbitrary inclusion shape, Comput. Mech. 55 (5) (2015) 963–981.

[9] Z. Liu, M.A. Bessa, W.K. Liu, Self-consistent clustering analysis: An efficient multi-scale scheme for inelastic heterogeneous materials, Comput. Methods Appl. Mech. Engrg. 306 (2016) 319–341.

[10] Z. Liu, M. Fleming, W.K. Liu, Microstructural material database for self-consistent clustering analysis of elastoplastic strain softening materials, Comput. Methods Appl. Mech. Engrg. 330 (2018) 547–577.

[11] Z. Liu, O.L. Kafka, C. Yu, W.K. Liu, Data-driven self-consistent clustering analysis of heterogeneous materials with crystal plasticity, in: Advances in Computational Plasticity, Springer, 2018, pp. 221–242.

[12] G. Cheng, X. Li, Y. Nie, H. Li, FEM-cluster based reduction method for efficient numerical prediction of effective properties of heterogeneous material in nonlinear range, Comput. Methods Appl. Mech. Engrg. 348 (2019) 157–184.

[13] Y. Nie, G. Cheng, X. Li, L. Xu, K. Li, Principle of cluster minimum complementary energy of FEM-cluster-based reduced order method: fast updating the interaction matrix and predicting effective nonlinear properties of heterogeneous material, Comput. Mech. (2019) 1–27.

[14] K. Wang, W. Sun, Q. Du, A cooperative game for automated learning of elasto-plasticity knowledge graphs and models with AI-guided experimentation, Comput. Mech. (2019) 1–33.

[15] T. Kirchdoerfer, M. Ortiz, Data-driven computing in dynamics, Internat. J. Numer. Methods Engrg. 113 (11) (2017) 1697–1710.

[16] T. Kirchdoerfer, M. Ortiz, Data driven computing with noisy material data sets, Comput. Methods Appl. Mech. Engrg. 326 (2017) 622–641.

[17] S. Conti, S. Muller, M. Ortiz, Data driven problems in elasticity, Arch. Ration. Mech. Anal. 229 (1) (2017) 79–123.

[18] R. Eggersmann, T. Kirchdoerfer, S. Reese, L. Stainier, M. Ortiz, Model-free data-driven inelasticity, Comput. Methods Appl. Mech. Engrg. 350 (2019) 81–99.

[19] S. Tang, G. Zhang, H. Yang, Y. Li, W.K. Liu, X. Guo, MAP123: A data-driven approach to use 1D data for 3D nonlinear elastic materials modeling, Comput. Methods Appl. Mech. Engrg. 357 (2019) 112587.

[20] H. Yang, X. Guo, S. Tang, W.K. Liu, Derivation of heterogeneous material laws via data-driven principal component expansions, Comput. Mech. (2019) 1–15.

[21] B. Gao, Y. Li, T.F. Guo, X. Guo, S. Tang, Void nucleation in alloys with lamella particles under biaxial loadings, Extreme Mech. Lett. 22 (2018) 42–50.

[22] B. Gao, G. Zhang, T. Guo, C. Jiang, X. Guo, S. Tang, Voiding and fracture in high-entropy alloy under multi-axis stress states, Mater. Lett. 237 (2019) 220–223.

[23] B. Gao, Q. Xiang, T. Guo, X. Guo, S. Tang, X.X. Huang, In situ TEM investigation on void coalescence in metallic materials, Mater. Sci. Eng. A 734 (2018) 260–268.

[24] L. Rosati, N. Valoroso, A return map algorithm for general isotropic elasto-visco plastic materials in principal space, Internat. J. Numer. Methods Engrg. 60 (2) (2004) 461–498.